A pipeline for multidimensional confocal analysis of mitochondrial morphology, function and dynamics in pancreatic β-cells

Ahsen Chaudhry[1,2,*], Rocky Shi[1,2,*] and Dan S. Luciani[1,2,#]

[1]*Department of Surgery, University of British Columbia, Vancouver, BC, Canada*

[2]*BC Children's Hospital Research Institute, Diabetes Research Group, Vancouver, BC, Canada*

*These authors contributed equally.

[#]**Corresponding Author:**

Dan S. Luciani, PhD

University of British Columbia

BC Children's Hospital Research Institute

A4-183, 950 W. 28th Avenue

Vancouver, BC, V5Z 4H4, Canada

Phone: (+1) 604-875-2000 ext. 6170

Fax: (+1) 604-875-2373

Email: dluciani@bcchr.ca

Key Words: Cell metabolism; diabetes; fluorescence microscopy; image analysis; live-cell imaging

Abbreviations: AR, aspect ratio; FF, form factor; GTO, ground truth object; mito-PAGFP, mitochondria-targeted photoactivatable green fluorescent protein; mito-YFP, mitochondria-targeted yellow fluorescent protein; MTG, MitoTracker Green; TMRE, tetramethylrhodamine, ethyl ester; PSF, point-spread function; SPADE, Spanning-tree progression analysis of density-normalized events

ABSTRACT

Live-cell imaging of mitochondrial function and dynamics can provide vital insights into both physiology and pathophysiology, including of metabolic diseases like type 2 diabetes. However, without super-resolution microscopy and commercial analysis software it is challenging to accurately extract features from dense multi-layered mitochondrial networks, such as those in insulin-secreting pancreatic β-cells. Motivated by this, we developed a comprehensive pipeline, and associated ImageJ plugin, that enables 2D/3D quantification of mitochondrial network morphology and dynamics in mouse β-cells, and by extension other similarly challenging cell-types. The approach is based on standard confocal microscopy and shareware, making it widely accessible. The pipeline was validated using mitochondrial photo-labelling and unsupervised cluster analysis, and is capable of morphological and functional analyses on a per-organelle basis, including in 4D (*xyzt*). Overall, this tool offers a powerful framework for multiplexed analysis of mitochondrial state/function, and provides a valuable resource to accelerate mitochondrial research in health and disease.

INTRODUCTION

Mitochondria are the main energy producing organelle of eukaryotic cells and are essential for a diverse range of cellular functions, including ATP synthesis, Ca^{2+} homeostasis, ROS signaling, and the control of apoptotic cell death (1, 2). Microscopy has been instrumental in unraveling intricacies of mitochondrial biology and their diverse roles in cellular physiology and pathophysiology. Electron microscopy has provided fundamental insights into mitochondrial ultrastructure and cellular distribution in health and disease but requires cell fixation and only provides a static snapshot. In contrast, fluorescence microscopy of live cells, labeled with mitochondria-targeted fluorescent proteins or dyes, has revealed that mitochondria are highly dynamic and motile organelles that undergo frequent fusion and fission events (3-5). Mitochondrial dynamics and network morphology vary in different cellular states, and are important for the function and quality control of the organelle, as well as overall cell health and adaptation to stress (1). Healthy mitochondria are generally mobile, tubular in shape and exist in complex networks, whereas cells undergoing profound stress or entering apoptosis often display swollen and fragmented mitochondria, marked by concurrent disruption of metabolism, membrane potential, ROS levels, and Ca^{2+} signalling (6-8). Quantitative imaging-based assessment of mitochondrial morphology and dynamics can therefore provide valuable insights into cellular physiology and pathophysiology.

In pancreatic β-cells, mitochondria play an essential role in insulin secretion, which relies on ATP and other mitochondria-derived metabolites to both trigger and amplify insulin granule exocytosis in response to glucose and other nutrient stimuli (9). Dysfunction of β-cell mitochondria therefore results in loss of glucose-stimulated insulin secretion (10). Perturbations to mitochondria are also a common feature in insulin target tissues with impaired insulin signaling (11, 12). Mitochondria thus take center stage in both β-cell failure and insulin resistance and are an area of significant focus in efforts to understand the pathophysiology of type 2 diabetes (13-15). Mitochondria also exist as dynamic networks in β-cells. Fusion within the network may help protect β-cells from nutrient stress-induced apoptosis (6), and mitochondrial fragmentation, swelling and dysfunction are seen in β-cells from patients with type 2 diabetes and rodent models of diabetes (15-18). Normal insulin secretion may also be influenced by β-cell mitochondrial dynamics (19-21), but exactly how networking of the organelle relates to its metabolic capacity in

75 healthy β-cells or during conditions of moderate nutrient excess remains unclear and warrants
76 further investigation.

77 Most types of microscopy can detect the prominent morphological differences between
78 healthy and severely stressed mitochondria with relative ease. It is, however, much more
79 challenging to accurately quantify subtle changes in mitochondrial dynamics, or perform 3D
80 analysis of the full mitochondrial network. This is particularly difficult in cells with a dense
81 mitochondrial network that spans several layers, such as β-cells (6, 18). Although methods have
82 been published that integrate 3D confocal imaging and analysis of mitochondria, these generally
83 use commercial software packages and/or are optimized for relatively flat cell types (22, 23). This
84 is likely one reason why there are only few quantitative analyses of β-cell mitochondrial dynamics,
85 and why full 3D investigations of β-cell mitochondria are limited to a small number of examples
86 using super-resolution approaches, such as 4π-microscopy (18, 24).

87 To facilitate progress in the important area of mitochondrial biology and dynamics we
88 present here a pipeline for quantitative multidimensional analysis of mitochondria that is based on
89 standard confocal fluorescence microscopy and the open source image analysis platform
90 ImageJ/Fiji (25, 26). In this, we identify a superior method for accurate identification of individual
91 mitochondria within dense networks, and we outline a framework for quantitative description of
92 mitochondrial morphology and network characteristics. Applying this pipeline to clonal MIN6 β-
93 cells and primary mouse β-cells, we quantitatively distinguish mitochondrial morphologies,
94 including the functional and morphological changes to physiological and pathophysiological
95 stimuli. Additionally, we discuss the pros and cons of 2D and 3D imaging approaches, identify
96 image processing steps required for accurate mitochondrial analysis in 3D, and apply these to
97 quantitate distinct 3D β-cell network morphologies. Finally, we extend our analysis to 4D by
98 including time-lapse data, and we demonstrate the feasibility of using the pipeline to quantitate the
99 dynamics of the entire three-dimensional mitochondrial network in live cells.

100

101 **RESULTS AND DISCUSSION**

102 ***Overall workflow & general considerations***

103 Fluorescence confocal analysis of mitochondria in live cells involves several general steps, each
104 of which is important for high-quality results (Figure 1). As a starting point, the cells must be
105 cultured on glass coverslips, or other vessels, that are appropriate for confocal microscopy. The

106   mitochondria should then be labelled using carefully chosen mitochondria-targeted fluorescent

107   proteins or organic dyes (27), and the image acquisition should be optimized and carried out in a

108   manner that provides sufficiently high resolution and image quality for accurate analysis. Because

109   these factors and general steps can vary between specific experiments and microscope systems, an

110   extensive discussion falls beyond the scope of this paper. The imaging parameters and conditions

111   we have used are detailed in Materials and Methods. Our focus in the following will be on the

112   post-acquisition steps that are critical for accurate morphological analysis of mitochondria in the

113   confocal images.

114   Image acquisition and analysis can be done in 2D or 3D, and by further extending this to

115   include time-lapse capture, important information can be extracted about mitochondrial dynamics.

116   The choice between these imaging modes may be influenced by several considerations, including

117   the type and thickness of the cell, the specific parameters to be quantified, and the biological

118   questions being asked. For instance, we will discuss later how some 2D analyses of relatively thick

119   cells, such as pancreatic β-cells, can be associated with inaccuracies that may be mitigated by a

120   full 3D analysis of the mitochondrial network. In all cases, accurate quantification of mitochondrial

121   features involves image processing steps and identification of the mitochondrial objects in the

122   image. Morphological features can then be extracted using appropriate 2D or 3D shape descriptors,

123   while mitochondrial networking can be assessed through skeletonization analysis. In this latter

124   process, the binarized mitochondria are converted into topological skeletons (the thinnest form

125   that is equidistant to its edges) and the branches of the skeleton are analyzed. In the following, we

126   describe each of these post-acquisition steps and identify a number of "best approaches", to build

127   a pipeline for accurate multidimensional analysis of mitochondria that we also implement and

128   make available in a comprehensive Mitochondria Analyzer plugin for ImageJ/Fiji (28).

129

130   ***Image thresholding and identification of mitochondria***

131   Before accurate morphological analysis of fluorescently–labeled mitochondria can be done, it is

132   essential that: i) the mitochondrial population is correctly identified in the images, and ii) the

133   individual mitochondrial units can be distinguished within the dense mitochondrial network. For

134   this critical step, a thresholding process based on analysis of the intensity histogram is used to

135   distinguish pixels with "true" fluorescent signal from background signal. This process also groups

136   any identified positive pixels that are connected into discrete objects (i.e. mitochondria) that can

137   be analyzed further. Thresholding approaches can be broadly categorized as either 'Global' or

138   'Local', which identify positive pixels based on the histogram of the entire image or on dynamic

139   analyses of image sub-regions, respectively (22, 29). Global thresholding tends to be the most

140   commonly used approach, but this may reflect its relative ease of use rather than accuracy.

141   To identify the most suitable thresholding strategy for mitochondrial identification, we

142   compared the performance of the Global and Local threshold methods available for ImageJ/Fiji on

143   images of primary islet cells stained with MitoTracker dye. This was judged on the ability to

144   preserve mitochondrial structural detail while minimizing capture of background signal. For

145   optimal results, all images were pre- and post-processed to reduce noise (see Materials &

146   Methods). Among the Global-based algorithms in the ImageJ/Fiji "Auto Threshold" command,

147   we qualitatively estimated that the Default method performs similar to, or in several cases better

148   than, the other Global algorithms (Figure S1).

149   The Local thresholding methods we tested included the Mean, Median, and Mid-grey

150   algorithms (part of the "Auto Local Threshold" command), as well as the Weighted Mean method

151   (also called Adaptive threshold), which is available through a separate plugin (30) (Figure S2).

152   These Local methods compute a threshold for each pixel in the image and require the definition of

153   two parameters: a block size and a C-value. The block size specifies the size of the region around

154   each pixel for which the histogram is analyzed and should be chosen based on the size of the

155   objects of interest for the best results (30). The C-value provides an offset to the threshold and

156   helps strike a balance between minimizing noise detection and incorrectly splitting objects into

157   smaller pieces (30, 31). Using the Adaptive threshold method for optimization, we found that the

158   ideal C-value depended on the image's signal-to-noise contrast and needed to be empirically

159   determined. For each set of images that has been acquired and processed in a similar manner, we

160   therefore recommend that various combinations of block size and C-values should be tested on a

161   representative image to determine the best combination. The optimized parameters can then be

162   used to threshold all images in the group similarly (Figure S2, Supplemental Methods for details).

163   Among the Local threshold approaches, our assessment was that the Mean and Adaptive threshold

164   methods best captured mitochondrial structure, and that the Adaptive threshold further tended to

165   identify less noise (Figure S2B).

166   A side-by-side comparison indicated that Local (Adaptive) thresholding resolves

167   mitochondria better than Global thresholding, which appears to capture more out-of-focus signal

168 and/or noise, and therefore erroneously merges adjacent objects (Figures 2A & B). For a more
169 stringent and quantitative evaluation, we used mitochondria-targeted photoactivatable GFP (mito-
170 PAGFP) to selectively photo-label single mitochondria and identify truly contiguous organelles
171 within dense regions of the network (4, 5). As exemplified in Figure 2B, and quantified in Figure
172 2C (see also Figure S3), Adaptive thresholding was indeed better at delineating photo-labeled
173 mitochondria, and distinguishing closely adjacent parts of the network that are physically separate.
174 In contrast, the Global threshold algorithm consistently overestimated the mitochondrial size.
175 Taken together, these comparisons established that using Adaptive thresholding, with empirically
176 optimized parameter values, is a superior approach for accurate identification of fluorescently
177 labeled β-cell mitochondria.

178

179 *Two-dimensional analysis of mitochondrial morphology and network connectivity*
180 After careful image thresholding, the next step is to quantify the morphological features of the
181 identified mitochondrial objects. We therefore identified a comprehensive set of parameters to
182 capture and mathematically describe key aspects of the mitochondrial morphology. For 2D
183 analysis, we characterize mitochondrial size by area and perimeter, while mitochondrial shape is
184 defined by form factor (FF) and aspect ratio (AR). We evaluate the overall connectivity and
185 morphological complexity of the mitochondrial network based on the skeletonized network, and
186 quantify this by the number of branches, the number of branch junctions, as well as total
187 (accumulated) length of branches in the skeleton. Figure 3 summarizes the various parameters and
188 indicate how they change with various morphologies.

189   To evaluate the ability of this approach to measure and distinguish mitochondrial
190 morphologies, we transfected MIN6 cells with mito-YFP and generated an image-set consisting
191 of 2D slices from 84 cells. We then divided the cells into three different categories based on visual
192 inspection of their mitochondria: 1) a "fragmented" group, characterized by small round
193 mitochondria and little branching; 2) a "filamentous" group, with highly connected networks of
194 long/filamentous mitochondria; and 3) an "intermediate" group of cells, containing a mixture of
195 punctate and longer tubular mitochondria. As shown in Figure 4, analysis of the 2D images resulted
196 in quantitative morphological and networking parameters that differed significantly between the
197 three groups. Of note, a more in-depth comparison of the two shape descriptors revealed that FF
198 required smaller sample sizes than AR to detect differences between the three morphological sub-

7

199 types, and seemed particularly well-suited for distinguishing between cells with filamentous and

200 intermediate mitochondrial morphologies (Figure S4). Likely, this is because AR only measures

201 elongation, whereas FF incorporates the perimeter and therefore is more sensitive to curvature and

202 the irregular shapes of filamentous mitochondria (Figure S4B). Collectively, these results

203 demonstrate that our combined approach for image processing, thresholding, and analysis enables

204 quantitative identification and comparison of mitochondrial morphological sub-types.

205

206 *Validation of morphometric quantifications and classifications by unsupervised clustering*

207 Next, we further tested our pipeline by using Spanning-tree Progression Analysis of Density-

208 normalized Events (SPADE) (32, 33) to obtain an unbiased classification of our test images. The

209 morphological parameters that had been calculated from our image set of 84 mito-YFP-expressing

210 MIN6 cells (shown in Figure 4) were loaded into SPADE, which used these to generate a

211 population tree in which each node represents a cell (Figure 5A). This SPADE tree was then

212 subdivided into 3 cell populations based on automatic classification of their mitochondrial features

213 (Figure 5A; see Materials and Methods for details). When images from each of the three SPADE-

214 identified groups were subsequently examined, the mitochondria in each group were noticeably

215 dissimilar in appearance (Figure 5B), and comparative analysis revealed that there were significant

216 differences in all the morphological descriptors (Figure 5C & D). The morphometric data indicated

217 that SPADE Subgroups 1, 2, and 3 corresponded to cells with filamentous, intermediate, and

218 fragmented mitochondria, respectively. This was confirmed by an 88% match between the

219 unsupervised SPADE clustering and our manual grouping of the cells. Together, these results

220 provide an unbiased validation of the applicability and robustness of our 2D pipeline for analysis

221 of mitochondrial network structure and complexity.

222

223 *Limitations of 2D mitochondrial analysis*

224 Our 2D analyses reliably measure mitochondrial morphology in an optical cross-section and can

225 provide valuable information regarding the state of the organelle. However, when cells are

226 relatively thick and tend to have a mitochondrial network that spans several layers, this approach

227 has its challenges and limitations. It is difficult to know if a given plane in a cell is truly

228 representative, and as illustrated by the green objects in Figure 6A the 2D appearance of a

229 mitochondrion will also depend on its orientation relative to the optical cross-section. Moreover,

8

230   a 2D image is unlikely to reveal the actual interconnectedness of the mitochondrial network. When

231   a mitochondrion spans multiple planes and intersects the focal cross-section at several points, it

232   can result in a notable misrepresentation of the morphology, as illustrated by the blue schematic

233   object in Figure 6A. That this also occurs in situ is demonstrated in the side-by-side 2D and 3D

234   visualization of a photo-labeled mitochondrion in Figure 6B & C. When viewed in 2D, the

235   localized photo-activation of mito-PAGFP seemed to label four small and distinct mitochondria

236   (Figure 6B; shown in green), but a full 3D reconstruction revealed that it was in fact one continuous

237   organelle (Figure 6C), consistent with diffusion-mediated distribution of GFP within the lumen.

238   Another inherent limitation of 2D analysis is that it does not allow direct quantitation of

239   the total mitochondrial mass. Cross-sectional area has been used to estimate mass in relatively flat

240   cells like neurons and fibroblasts where mitochondria are confined to a limited number of planes

241   (22, 34). However, this approximation is less appropriate for thicker cells, including β-cells. A

242   common alternative, intended to capture as much of the mitochondrial network as possible,

243   involves acquiring a stack of z-slices and projecting these into a single plane for faster and simpler

244   analysis (6, 23). Such projections contain information from the whole network, but in voluminous

245   cells this will erroneously merge overlapping mitochondria and produce indiscriminate clusters in

246   the resulting image.

247   As the importance of mitochondrial dynamics and its implication for cellular health and

248   disease has become more apparent, there is also an increasing need for more comprehensive

249   characterization of the organelle. Accordingly, there will inevitably be instances where the caveats

250   of 2D analysis we discussed above become restricting. To enable more precise quantification of

251   mitochondrial volume and network structure we therefore expanded our pipeline to include a

252   complete 3D representation and analysis.

253

Three-dimensional imaging and analysis of mitochondria

255   Full 3D reconstruction of mitochondria can be accomplished by taking a stack of serial slices

256   throughout the volume of the cell and integrating them with software such as ImageJ/Fiji.

257   However, there are technical challenges and constraints specifically associated with 3D imaging.

258   Foremost of these is that the maximum axial resolution (z-axis) of confocal microscopes is

259   approximately 500-800 nm, which is almost three times worse than the lateral (*xy*-plane) (35, 36).

260   As mitochondria are often less than 1 micron in diameter they approach this limit (18). This can

9

261 lead to a distorted appearance of imaged mitochondria, particularly in the z-axis where it causes

262 artificial stretching and blending of signal from objects in close vertical proximity to each other.

263 In the following section we discuss steps that can be taken to mitigate some of these caveats and

264 improve 3D results.

265

266 *Image acquisition and processing requirements for accurate 3D analysis*

267 An important first consideration when acquiring a stack of images for 3D analysis is the z-distance

268 between adjacent imaging planes. If the spacing is too large the final reconstruction will be

269 inaccurate. On the other hand, over-sampling will take unnecessary time, increase photo-toxicity,

270 and require additional resources for image storage and analysis. The distance between serial

271 sections should therefore be set according to the optimal Nyquist sampling rate, which provides

272 the ideal density of information to permit accurate digital reconstruction of an object (37). The

273 Nyquist distance can be calculated using online resources (38).

274 Even under optimal conditions, a confocal image will be affected by inherent diffraction-

275 induced distortion of the imaged object. This distortion can be represented by a point-spread

276 function (PSF) and then computationally corrected by using deconvolution algorithms. By

277 removing the effects of the PSF, the deconvolution process provides a more correct representation

278 of the underlying object and also helps eliminate out-of-focus light and/or noise in the image (36).

279 In Figure 7 we illustrate this and use the free DeconvolutionLab2 module for ImageJ/Fiji and the

280 commercial deconvolution software, Huygens Professional (SVI), to test the effect of

281 deconvolution on 3D-stacks of mitochondria (see Materials and Methods for details). As seen in

282 Figure 7A, mitochondria in the raw image stack have approximately 2-3x greater diameter in the

283 *xz*-view than in the *xy*-view, which illustrates the z-stretching. The deconvolution algorithms help

284 reduce this distortion, remove noise, and improve the contrast and separation of adjacent objects

285 (Figure 7A and Figure S5). In general, we found that the Huygens deconvolution package reduced

286 axial stretching more effectively than the ImageJ DeconvolutionLab2 module. By and large,

287 however, both deconvolution algorithms significantly increased the quality of 3D mitochondrial

288 network reconstructions compared to the raw confocal images (Figure 7B). Deconvolution also

289 affected subsequent 3D quantifications of mitochondrial number, shape, and size in a way that

290 indicated superior separation of individual mitochondria within the full population (Supplemental

291 Table 1; see discussion of the 3D analysis parameters below). In summary, these results

10

292   demonstrate that deconvolution of the raw confocal image stacks helps mitigate limitations of 3D

293   imaging and is a necessary step for accurate reconstruction and quantification of the full

294   mitochondrial network.

295

296   ***Three-dimensional quantification of mitochondrial morphology and network connectivity***

297   When a high-quality representation of the full mitochondrial network has been generated,

298   ImageJ/Fiji can be used to extract information about the 3D morphology and connectivity by the

299   same general principles previously discussed for 2D. Mitochondrial size in 3D is represented by

300   volume and surface area, while shape is characterized by the sphericity of the mitochondrial object.

301   The complexity of the 3D network is quantified by the same branch parameters used for 2D (see

302   Figure 3 for a summary). Analogous to our 2D analyses, we evaluated our 3D approach by

303   generating a set of image stacks from mito-YFP-expressing MIN6 cells, and grouping these as

304   fragmented, filamentous, or intermediate based on the visual appearance of the reconstructured

305   mitochondrial networks (Figure 8A). Quantification using ImageJ/Fiji (See Figure 9 and Materials

306   & Methods for details) showed that the number of mitochondria per cell and their average

307   sphericity progressively increased, while the average mitochondrial volume decreased, as we move

308   from filamentous to intermediate to fragmented morphologies (Figure 8B). In contrast, the total

309   mitochondrial volume of each cell remained constant, highlighting that significant morphological

310   heterogeneity can occur independent of changes to mitochondrial mass (Figure 8B). In the

311   skeletonized network the number of branches and branch junctions progressively decreased,

312   illustrating that mitochondrial fragmentation, not surprisingly, is associated with a reduction in

313   overall network complexity (Figure 8C & D). Together, the above results and discussions

314   demonstrate how standard confocal imaging can be combined with ImageJ/Fiji-based processing

315   and analysis, to quantify volume, morphology, and connectivity of the entire mitochondrial

316   network in pancreatic β-cells. To our knowledge, full 3D characterization of live β-cell

317   mitochondria has previously only been done at this level using specialized super-resolution

318   imaging techniques (18, 24).

319

320   ***Pipeline Summary***

321   Figure 9 illustrates the overall pipeline for 2D and 3D mitochondrial analysis. In summary, 2D

322   image slices or 3D image stacks are first acquired, and the latter deconvolved prior to analysis. In

11

323 ImageJ/Fiji, deconvolution of 3D stacks is done using the DeconvolutionLab2 module (39) and if

324 desired, the 3D stack can be visualized using the "3D Viewer" or "Volume Viewer" functions.

325 Alternatively, 3D deconvolution and visualization can be done using commercial software, such

326 as Huygens, if available to the user (Figure 7). For analysis, all images are then pre-processed

327 using the commands: "Subtract Background", "Sigma Filter Plus", "Enhance Local Contrast", and

328 "Gamma Correction". We then empirically test a range of block sizes and C-values for the

329 "Adaptive Threshold" command to establish the optimal values and use these as input when

330 applying the threshold algorithm. The resulting binarized images are post-processed using the

331 "Despeckle", "Remove Outliers", and "Fill 3D Holes" commands. At this stage, we recommend

332 comparing the final thresholded image to the original images as a quality control check of the

333 object identification and segmentation. The identified mitochondrial objects are then analyzed in

334 2D using "Analyze Particles", which provides mitochondrial count, area, perimeter, form factor

335 (FF), and aspect ratio (AR). For 3D analysis, we use the "3D Object Counter" and "3D Particle

336 Analyzer" (from the MorphoLibJ package) commands to quantify count, volume, surface area,

337 and sphericity. The thresholded objects are then converted into skeletons using "Skeletonize

338 (2D/3D)", and we apply the "Analyze Skeleton" command to obtain the number of skeletons,

339 number of branches, length of branches, and number of branch junctions in the 2D or 3D network.

340 Additional details and parameter values can be found in Materials and Methods.

341

342 *Quantifying physiological and pathophysiological changes to mitochondrial morphology and*

343 *networking*

344 Having established and validated the mitochondrial analysis pipeline, we next used it to

345 characterize mitochondrial changes under relevant physiological and pathophysiological

346 conditions. As a test of acute functional responses, primary mouse β-cells were cultured in either

347 basal (3 mM) or stimulatory (17 mM) glucose for 1 hour and co-stained with MitoTracker green

348 (MTG) and the mitochondrial membrane potential-sensitive dye TMRE (Figure 10A). The MTG

349 fluorescence is insensitive to changes in mitochondrial polarization and served as the signal for

350 mitochondrial detection and morphological characterization (40). The TMRE intensity provided a

351 simultaneous readout of the activity of the individual mitochondrial units, and as expected

352 stimulatory glucose increases the TMRE/MTG intensity ratio (Figure 10B). By visual inspection

353 there were no obvious differences in mitochondrial morphology between the cells in low and high

12

354 glucose (Figure 10A), but quantitative analysis revealed a number of significant effects (Figure

355 10C & D). Despite no change to total mitochondrial area, glucose stimulation increased the number

356 of mitochondria, reduced their average size (area and perimeter) and made them more round

357 (decreased form factor); all of which suggests increased mitochondrial fission (Figure 10C). This

358 was further supported by skeletonization analysis, which showed that stimulatory glucose caused

359 an overall reduction in mitochondrial network connectivity (decreased branch parameters) (Figure

360 10D). This experiment agrees with previous reports linking drp1-dependent mitochondrial fission

361 to glucose-stimulated insulin secretion (19, 20), and demonstrates that our analysis pipeline is

362 sensitive enough to allow quantitative detection of subtle physiological changes to mitochondrial

363 morphology and networking.

364 As an example of a full 3D application, we quantified the mitochondrial changes in

365 palmitate-treated MIN6 cells; an *in vitro* model of the β-cell lipotoxicity associated with obesity

366 and type 2 diabetes. As expected from previous 2D analyses (6) we observed a fragmentation of

367 the mitochondrial network following treatment with a high concentration of palmitate (Figure S6).

368 This pathophysiological stress response did not affect total mitochondrial volume but was clearly

369 reflected in all parameters describing the 3D shape and size of individual mitochondrial units

370 (Figure S6). Comparing the 2D morphological changes associated with 1 hour of glucose

371 stimulation and 6 hours of palmitate exposure, it is interesting to note that palmitate treatment

372 reduced AR by 26% and FF by 29%, while glucose stimulation only decreased AR and FF by 4%

373 and 12%, respectively. This suggests that physiological fission generates daughter mitochondria

374 that largely retain their shape, in contrast to the more pronounced stress-induced fragmentation,

375 which also causes a striking rounding of the smaller organelles.

376

377 *Four-dimensional analysis of mitochondrial dynamics*

378 At any given time, the overall structure of a mitochondrial network reflects the net balance of

379 fusion and fission between individual mitochondria. These are dynamic, energy-dependent,

380 processes that involve mitochondrial movement, and coordinated actions of proteins that mediate

381 fusion of the outer and inner membranes, or constriction and splitting of the organelle (2). Based

382 on static image analysis alone it can be difficult to know the reason for a change in morphometry.

383 For instance, a more connected and elongated network can be the result of an increase in fusion

384 events, a decrease in fission activity, or a combination of both. To further understand the

13

385 underlying changes, it can therefore be valuable to monitor mitochondrial movement,

386 morphological changes, and organelle interactions in real-time. In practical terms, this requires

387 that image acquisition can be repeated at sufficiently frequent intervals, and that the analysis is

388 extended to the time-domain. Previous studies have applied these principles to 2D images to

389 provide important insights regarding mitochondrial dynamics and turnover in pancreatic β-cells

390 (3, 6).

391   Here, we tested the feasibility of recording and quantifying the time-dependent dynamics

392 of the full 3D mitochondrial network (i.e. an extension to 4D analysis). For this, we expressed

393 mito-YFP in MIN6 cells and imaged these in a stage-top incubator on the confocal microscope.

394 3D time-lapse data were generated by acquiring z-stacks of the cells at regular time-intervals

395 (every 45 s) for a period of 30 minutes. At the 13-minute mark, we added a high concentration of

396 the mitochondrial uncoupling agent, FCCP, with the purpose of inducing a relatively rapid change

397 in mitochondrial dynamics and architecture. As seen in Figure 11 and Supplemental Video 1, the

398 FCCP triggered a rapid, and dramatic, loss of mitochondrial connectivity along with an increase

399 in the number of organelles. Interestingly, there was also a transient decrease in both average and

400 total mitochondrial volume, which indicates an initial contraction and shrinking of the

401 mitochondrial fragments followed by significant swelling; a known response to stress and osmotic

402 shock (41). The abrupt and severe deterioration of the mitochondrial network likely reflects the

403 induction of apoptosis due to profound damage from high levels of FCCP.

404   With this proof-of-principle experiment we have established the feasibility of analyzing

405 the temporal dynamics of a full mitochondrial network using standard confocal microscopy. A

406 powerful next step could be to combine this 4D approach with other tools such as photo-labeling

407 and tracking of individual organelles, to generate even more complete and in-depth knowledge of

408 the events that shape the mitochondrial network in health and disease.

409

410 **CONCLUSION & PERSPECTIVES**

411 Most aspects of cellular function and survival are linked to mitochondrial physiology or signals

412 originating from the organelle, and in these contexts the importance of mitochondrial morphology

413 and dynamics has become evident (1, 2). The integrity of the organelle itself, and by extension the

414 metabolic health of the cell, depends on the capacity for mitochondrial adaptation to stress and on

415 selective turnover of damaged parts of the network by mitophagy (3). These processes rely on

416   mitochondrial fusion and fission dynamics, which require sensitive live-cell imaging approaches

417   to study (42). Our current understanding of mitochondrial dynamics in pancreatic β-cells has also

418   been based largely on such imaging approaches (3, 6). However, it is challenging to accurately

419   quantify β-cell mitochondrial morphometry and dynamics by fluorescence microscopy, and many

420   important questions remain unanswered.

421   In the previous sections, we established a comprehensive set of methods for quantitative

422   image analysis and 'morphofunctional' characterization of mitochondria based on standard

423   confocal microscopy and the ImageJ/Fiji shareware. The robustness of these approaches was

424   validated in several ways, including by unsupervised data clustering. We demonstrated the

425   applicability of the resulting pipeline for cells with dense multi-layered mitochondria by

426   conducting detailed 2D and 3D morphometric analyses of β-cells, and further extended these to

427   4D time-lapse imaging with the accuracy needed for quantitative assessment of network dynamics.

428   To help researchers implement these methods, we have also built our analysis pipeline into a plugin

429   for ImageJ/Fiji called Mitochondria Analyzer. The plugin is publicly available (28) and includes

430   a graphical user interface to facilitate pre-processing, parameter optimization, image thresholding

431   and automated morphofunctional analysis of mitochondrial images or image stacks, according to

432   the work-flow we have presented (Figure 9).

433   When testing the pipeline, we demonstrated the capability for multi-parameter

434   characterization by performing 2D analyses of β-cells co-stained with MTG and TMRE for

435   simultaneous recordings of changes to mitochondrial morphology and membrane potential.

436   However, the pipeline can in principle be applied to any number of mitochondrial parameters,

437   provided they can be jointly imaged and then quantified using shape- and intensity-based

438   descriptors. We therefore predict that the same type of analysis using a stable mitochondrial label

439   combined with one or more spectrally distinct fluorescent biosensors, e.g. for mitochondrial redox

440   state, matrix Ca^{2+} or pH, could provide valuable insights into physiological and pathophysiological

441   structure-function relationships in mitochondria. Importantly, the analysis pipeline treats all

442   identified objects separately, and can therefore extract the morphological and functional

443   descriptors on a per-mitochondria basis. In the previous sections we presented our results based

444   on the cellular averages, but the same data-sets contain the descriptors associated with thousands

445   of individual mitochondria and can be mined for a wealth of information about morphometry-

446   physiology correlations and heterogeneity at the organelle level (43, 44). It should also be

447 emphasized that the practical considerations and best-practices we have discussed, and
448 incorporated into our pipeline, are not restricted to β-cell analyses, but can also be applied to other
449 cell types.

450   Finally, the pipeline can in principle also be used to investigate fluorescently labelled
451 organelles other than mitochondria, provided that appropriate thresholding/analysis parameter
452 adjustments can be made. The importance of inter-organelle contacts for cellular function and
453 health are becoming clear, as is the highly complex and dynamic nature of the "organelle
454 interactome" (45-47). Within the technical boundaries associated with standard confocal
455 microscopy, the analysis approaches we have described here can help most research laboratories
456 achieve the level of accuracy needed to explore internal mitochondrial network interactions, and
457 likely also the mitochondrial relationship with other organelles, as we work to clarify the sub-
458 cellular basis of diabetes and other diseases.

459

MATERIALS AND METHODS
460

Reagents
461

462 Collagenase type XI (#C7657), Tetramethylrhodamine Ethyl Ester (TMRE, #87917), D-glucose
463 (#G7528), Bovine Serum Albumin (BSA, #A7030), FCCP (#C2920) and palmitic acid (#P5585)
464 were purchased from Sigma-Aldrich (St. Louis, Missouri). MitoTracker Deep Red FM
465 (#M224726), MitoTracker Green FM (MTG, #M7514), Hoechst 33342 (#H3570), RPMI 1640
466 (#11879), Dulbecco's Modified Eagle's Medium (DMEM, #11995), Fetal Bovine Serum (FBS,
467 #10438), Trypsin-EDTA (#25300), Penicillin-Streptomycin 10,000 U/mL (#15140), and HBSS
468 (#14185) were purchased from Life Technologies/Thermo Fisher Scientific (Carlsbad, California).
469 Dimethyl sulfoxide (DMSO, #BP231) was purchased from Fisher Scientific (Waltham,
470 Massachusetts). Minimum Essential Media (MEM, #15-015-CV) was purchased from Corning
471 (Corning, New York). The mitochondria-targeted YFP (mito-YFP) and mitochondria-targeted
472 photoactivatable GFP (mito-PAGFP) plasmids were gifts from Dr. Mark Cookson (48) and Dr.
473 Richard Youle (Addgene #23348) (5), respectively.

474

Cell Isolation and Culture
475

476 MIN6 cells were cultured at 37°C and 5% CO_2 using complete DMEM supplemented with 10%
477 FBS and 2% Penicillin-Streptomycin. Culture media was replaced every 2 days and cells were

16

478   passaged upon reaching 70-80% confluency. To assess the effects of palmitate on mitochondrial

479   networks, cells were cultured for 6 hours in complete DMEM supplemented with either 1.5 mM

480   palmitate complexed to BSA in a 6:1 ratio, or BSA-only vehicle control.

481   Pancreatic islets were isolated from wild-type male mice of a mixed C57BL/6 and CD1

482   background using collagenase digestion and filtration-based purification, as previously described

483   (49). The isolated islets were hand-picked and allowed to recover overnight before being dispersed

484   into single cells and seeded on 25 mm glass coverslips (50). The islet cells were cultured in RPMI

485   completed with 10% FBS and 2% Penicillin-Streptomycin at 37ºC and 5% CO_2 for 4 days before

486   imaging. All animal procedures were approved by the University of British Columbia Animal Care

487   Committee.

488

489   *Cell Transfection and Mitochondrial Labeling*

490   MIN6 cells were seeded at a density of 2.0 x 10^5 on 25 mm glass coverslips (0.13-0.16 mm

491   thickness, VWR #16004-310) and incubated for 24 hours before being transfected with mito-YFP,

492   mito-dsRed, or mito-PAGFP plasmids using Lipofectamine® 2000 (Life Technologies #11668),

493   as per the manufacturer's protocol. All plasmids were expressed for at least 24 hours before

494   confocal microscopy.

495   To assess the effect of acute glucose exposure on mitochondrial morphology and

496   membrane potential, primary mouse islet cells were cultured for 60 minutes in completed RPMI

497   media containing 3 mM glucose or 17 mM glucose and then stained with 0.1 µg/mL Hoescht

498   33342, 50 nM MTG, and 25 nM TMRE for 30 min, followed by a wash with completed RPMI

499   immediately prior to imaging.

500

501   *Image Acquisition by Confocal Microscopy*

502   Live cells were imaged in a Tokai Hit INUBTFP-WSKM stage-top incubator at 37ºC on a Leica

503   SP8 Laser Scanning Confocal Microscope (Concord, Ontario, Canada). For 2D, images were

504   acquired using a 63x HC Plan Apochromatic water immersion objective (1.2 NA). Pixel size was

505   adjusted using the "Optimize" function in the Leica LASX Software and the pinhole size was 1.0

506   AU. For 3D acquisition, *z*-stacks were obtained using a 63x oil immersion objective (1.4 NA).

507   Pixel size (*x*, *y*) and *z*-spacing were adjusted as per the calculated optimal Nyquist sampling

508   parameters (38), and pinhole size was reduced to 0.75 AU. The *z*-step size generally varied

17

509 between 170-220 nm. Bi-directional scanning was enabled, and all images were acquired using at
510 least three frame averages. Laser power, detector filtering/gating, and gain were adjusted to
511 maximize signal without saturation, while also minimizing background signal, cross-fluorescence,
512 and photobleaching.

513

514 ***Time-Lapse 3D Imaging***
515 Time-lapse 3D (*xyzt*) imaging was performed on MIN6 cells transfected with mito-YFP plasmid.
516 Acquisition settings were established as above, and *z*-stacks were acquired every 45 s for 30 min.
517 The acquisition time for each stack was approximately 30 s. At the 13 min-mark, FCCP was added
518 to the chamber for a final concentration of 25 μM.

519

520 ***Mitochondrial labeling by Photoactivatable Green Fluorescent Protein***
521 MIN6 cells were co-transfected with mito-PAGFP and mito-dsRed 24 hours prior to imaging, as
522 described above. Mito-dsRed was visualized using a 561 nm excitation laser with emission
523 detected between 585 nm to 650 nm. Individual mitochondria were marked for photo-labeling
524 using the "Bleach Point" function in the Leica LasX software, and the PAGFP was activated using
525 a 405 nm laser pulse of 150 ms duration. The activated PAGFP was then imaged using a 488 nm
526 excitation laser with an emission range between 505 nm and 550 nm. All other imaging settings
527 were as described above.

528

529 ***Image Deconvolution***
530 Deconvolution of 3D and 4D stacks was performed in Huygens Professional version 16.10 (SVI)
531 using the CMLE (Classic Maximum Likelihood Estimation) algorithm with a Signal-to-Noise
532 Ratio of 7.0, maximum iterations of 40, and quality threshold of 0.001. For deconvolution in
533 ImageJ/Fiji, the "PSF Generator" plugin (51) was used to generate a theoretical PSF based on our
534 microscope parameters, and deconvolution was performed with the "DeconvolutionLab2" module
535 utilizing the Richardson-Lucy TV algorithm with regularization set to 0.0001 and maximum
536 iterations of 30 (39, 52).

537

538

539

Image Processing and Thresholding

540

541 The workflow and procedures for image processing and thresholding are summarized in Figure 9.

542 Using ImageJ/Fiji, 2D images or deconvolved 3D image stacks (operating on each slice in the

543 stack) were pre-processed using the following commands: 1) "Subtract Background" (radius =

544 1μm) to remove background noise; 2) "Sigma Filter Plus" (radius = 0.1 μm, 2.0 sigma) to reduce

545 noise and smooth object signal while preserving edges; 3) "Enhance Local Contrast" (block size

546 = 64, slope = 2.0 for 2D and 1.25 for 3D stacks) to enhance dim areas while minimizing noise

547 amplification; and 4) "Gamma Correction" (value = 0.80 for 2D and 0.90 for 3D) (29) to correct

548 any remaining dim areas. To identify mitochondria in the images, we evaluated multiple global

549 and local thresholding algorithms (Figure 2 and Figures S1-S3). Based on our comparisons, we

550 elected to use the "Adaptive Threshold" method (30). In the "Adaptive Threshold" plugin, block

551 size was set to an equivalent of 1.25 μm and the optimal C-value was empirically determined for

552 each image set (See Figure S2 for additional details). The thresholded images were then post-

553 processed using "Despeckle" and then "Remove Outliers" (radius = 0.15 μm^2) to remove residual

554 noise. For 3D stacks we additionally applied the "Fill 3D Holes" command from the "3D ROI

555 Manager" plugin (53).

556

2D Analysis of Mitochondrial Function, Morphology, and Network Characteristics

557

558 The approach for quantification of mitochondrial characteristics is summarized in Figure 9. For

559 2D analysis, the image was first processed and thresholded (see above) and the resulting binary

560 image was used as the input for the "Analyze Particles" command (Size = 0.06 μm^2-Infinity,

561 Circularity = 0.00-1.00), measuring for "Area", "Perimeter", and "Shape Descriptors". Form

562 Factor (FF) was derived as the inverse of the "Circularity" output value. For network connectivity

563 analysis, the "Skeletonize 2D/3D" command was applied to the thresholded image to produce a

564 skeleton map, and the "Analyze Skeleton" command was used to calculate the number of branches,

565 branch lengths, and branch junctions in the skeletonized network.

566 To simultaneously measure mitochondrial polarisation and morphology, islet cells were

567 co-stained with MTG and TMRE. Our threshold method was first applied to the MTG channel and

568 morphological analysis was done on the identified objects. Additionally, the "Analyze Particles"

569 command ("Add to Manager" option enabled) was used to convert the identified objects

570 (mitochondria) into regions of interest (ROIs). These ROIs were then superimposed onto the raw

19

571   images of the MTG and TMRE channels, and the MTG and TMRE intensities of each individual

572   mitochondrion were measured as the "Mean gray value" obtained via the "Analyze Particles"

573   command. The degree of mitochondrion polarisation was then expressed as the ratio of TMRE to

574   MTG intensity and correlated with mitochondrial morphology on a per-organelle basis.

575

3D Analysis of Mitochondrial Morphology and Network Characteristics

576

577   For 3D analysis, the image stacks were first deconvolved, pre-processed, and thresholded as

578   described above and summarized in Figure 9. Next, the "3D Object Counter" command (Size =

579    $0.6\,\mu m^3$-Infinity) was used to calculate the number of mitochondrial objects and produce a labelled

580   object map. The object map was subsequently used as an input for the "Particle Analyzer 3D"

581   command (part of the MorphoLibJ package) (54) to calculate the volume, sphericity (weighted by

582   volume of the object), and corrected surface area ("Crofton 13 directions" method) of each

583   mitochondrial object. Network connectivity analysis was performed on the skeletonized 3D

584   network using the same commands as 2D analysis. For 4D (*xyzt*) analysis, these 3D analysis steps

585   were performed on each stack obtained in the time-course acquisition.

586

Unsupervised Categorization of Mitochondrial Morphology using SPADE

587

588   Spanning-tree Progression Analysis of Density-normalized Events (SPADE v3.0) (32, 33) was

589   used to automatically classify 2D mitochondrial images into 3 different categories based

590   exclusively on their calculated morphological and network parameters. Briefly, mitochondrial

591   parameter data was transformed into a Flow Cytometry Standard (FCS) file using FlowJo V10 and

592   loaded into SPADE. A SPADE tree was created using default settings, without application of

593   arcsinh transformation or removal of outliers. The number of desired clusters was set equal to the

594   total number of images in the data set. The "Auto Suggest Annotation" function was then used to

595   partition the SPADE tree into 2 subgroups and the larger of these was subsequently auto-

596   partitioned again, resulting in a total of 3 subgroups. The data in these SPADE-identified groups

597   were then exported as CSV formatted files for statistical comparison.

598

Statistical analysis

599

600   All data were represented as mean ± standard error of the mean (SEM). Data were analyzed in

601   GraphPad Prism 6.0 software (La Jolla, California) using Student's t-test or One-way ANOVA,

602 followed by Sidak multiple comparison test as appropriate. Statistical significance was set at a

603 threshold of $p < 0.05$.

604

605 **ACKNOWLEDGEMENTS**

613

614 **AUTHOR CONTRIBUTIONS**

615 AC, RS and DSL all contributed to the design of methods and validations. AC and RS performed

616 the experiments and validations. AC, RS and DSL all analyzed/interpreted the data and wrote the

617 paper. AC developed the associated Mitochondria Analyzer plugin for ImageJ.

618

619 **COMPETING INTERESTS**

620 None of the authors have competing interests to declare.

621

622 **REFERENCES**

623 1.   Eisner V, Picard M, Hajnoczky G. Mitochondrial dynamics in adaptive and maladaptive
624 cellular stress responses. Nat Cell Biol. 2018;20(7):755-65.

625 2.   Pernas L, Scorrano L. Mito-Morphosis: Mitochondrial Fusion, Fission, and Cristae
626 Remodeling as Key Mediators of Cellular Function. Annu Rev Physiol. 2016;78:505-31.

627 3.   Twig G, Elorza A, Molina AJ, Mohamed H, Wikstrom JD, Walzer G, et al. Fission and
628 selective fusion govern mitochondrial segregation and elimination by autophagy. EMBO J.
629 2008;27(2):433-46.

630 4.   Twig G, Graf SA, Wikstrom JD, Mohamed H, Haigh SE, Elorza A, et al. Tagging and
631 tracking individual networks within a complex mitochondrial web with photoactivatable GFP. Am
632 J Physiol Cell Physiol. 2006;291(1):C176-84.

633   5.   Karbowski M, Arnoult D, Chen H, Chan DC, Smith CL, Youle RJ. Quantitation of
634   mitochondrial dynamics by photolabeling of individual organelles shows that mitochondrial fusion
635   is blocked during the Bax activation phase of apoptosis. J Cell Biol. 2004;164(4):493-9.

636   6.   Molina AJ, Wikstrom JD, Stiles L, Las G, Mohamed H, Elorza A, et al. Mitochondrial
637   networking protects beta-cells from nutrient-induced apoptosis. Diabetes. 2009;58(10):2303-15.

638   7.   Arnoult D. Mitochondrial fragmentation in apoptosis. Trends Cell Biol. 2007;17(1):6-12.

639   8.   Brookes PS, Yoon Y, Robotham JL, Anders MW, Sheu SS. Calcium, ATP, and ROS: a
640   mitochondrial love-hate triangle. Am J Physiol Cell Physiol. 2004;287(4):C817-33.

641   9.   Prentki M, Matschinsky FM, Madiraju SR. Metabolic signaling in fuel-induced insulin
642   secretion. Cell Metab. 2013;18(2):162-85.

643   10.   Silva JP, Kohler M, Graff C, Oldfors A, Magnuson MA, Berggren PO, et al. Impaired
644   insulin secretion and beta-cell loss in tissue-specific knockout mice with mitochondrial diabetes.
645   Nat Genet. 2000;26(3):336-40.

646   11.   Jheng HF, Tsai PJ, Guo SM, Kuo LH, Chang CS, Su IJ, et al. Mitochondrial fission
647   contributes to mitochondrial dysfunction and insulin resistance in skeletal muscle. Mol Cell Biol.
648   2012;32(2):309-19.

649   12.   Samuel VT, Shulman GI. The pathogenesis of insulin resistance: integrating signaling
650   pathways and substrate flux. J Clin Invest. 2016;126(1):12-22.

651   13.   Fex M, Nicholas LM, Vishnu N, Medina A, Sharoyko VV, Nicholls DG, et al. The
652   pathogenetic role of beta-cell mitochondria in type 2 diabetes. J Endocrinol. 2018;236(3):R145-
653   R59.

654   14.   Sharoyko VV, Abels M, Sun J, Nicholas LM, Mollet IG, Stamenkovic JA, et al. Loss of
655   TFB1M results in mitochondrial dysfunction that leads to impaired insulin secretion and diabetes.
656   Human molecular genetics. 2014;23(21):5733-49.

657   15.   Haythorne E, Rohm M, van de Bunt M, Brereton MF, Tarasov AI, Blacker TS, et al.
658   Diabetes causes marked inhibition of mitochondrial metabolism in pancreatic beta-cells. Nature
659   communications. 2019;10(1):2474.

660   16.   Anello M, Lupi R, Spampinato D, Piro S, Masini M, Boggi U, et al. Functional and
661   morphological alterations of mitochondria in pancreatic beta cells from type 2 diabetic patients.
662   Diabetologia. 2005;48(2):282-9.

663   17.   Lu H, Koshkin V, Allister EM, Gyulkhandanyan AV, Wheeler MB. Molecular and
664   metabolic evidence for mitochondrial defects associated with beta-cell dysfunction in a mouse
665   model of type 2 diabetes. Diabetes. 2010;59(2):448-59.

18.   Dlaskova A, Spacek T, Santorova J, Plecita-Hlavata L, Berkova Z, Saudek F, et al. 4Pi microscopy reveals an impaired three-dimensional mitochondrial network of pancreatic islet beta-cells, an experimental model of type-2 diabetes. Biochim Biophys Acta. 2010;1797(6-7):1327-41.

19.   Hennings TG, Chopra DG, DeLeon ER, VanDeusen HR, Sesaki H, Merrins MJ, et al. In vivo Deletion of Beta Cell Drp1 Impairs Insulin Secretion without Affecting Islet Oxygen Consumption. Endocrinology. 2018.

20.   Kabra UD, Pfuhlmann K, Migliorini A, Keipert S, Lamp D, Korsgren O, et al. Direct Substrate Delivery Into Mitochondrial Fission-Deficient Pancreatic Islets Rescues Insulin Secretion. Diabetes. 2017;66(5):1247-57.

21.   Park KS, Wiederkehr A, Kirkpatrick C, Mattenberger Y, Martinou JC, Marchetti P, et al. Selective actions of mitochondrial fission/fusion genes on metabolism-secretion coupling in insulin-releasing cells. J Biol Chem. 2008;283(48):33347-56.

22.   Nikolaisen J, Nilsson LI, Pettersen IK, Willems PH, Lorens JB, Koopman WJ, et al. Automated quantification and integrative analysis of 2D and 3D mitochondrial shape and network properties. PLoS One. 2014;9(7):e101365.

23.   Song W, Bossy B, Martin OJ, Hicks A, Lubitz S, Knott AB, et al. Assessing mitochondrial morphology and dynamics using fluorescence wide-field microscopy and 3D image processing. Methods. 2008;46(4):295-303.

24.   Plecita-Hlavata L, Lessard M, Santorova J, Bewersdorf J, Jezek P. Mitochondrial oxidative phosphorylation and energetic status are reflected by morphology of mitochondrial network in INS-1E and HEP-G2 cells viewed by 4Pi microscopy. Biochim Biophys Acta. 2008;1777(7-8):834-46.

25.   Schindelin J, Arganda-Carreras I, Frise E, Kaynig V, Longair M, Pietzsch T, et al. Fiji: an open-source platform for biological-image analysis. Nat Methods. 2012;9(7):676-82.

26.   Schneider CA, Rasband WS, Eliceiri KW. NIH Image to ImageJ: 25 years of image analysis. Nat Methods. 2012;9(7):671-5.

27.   Liu X, Yang L, Long Q, Weaver D, Hajnoczky G. Choosing proper fluorescent dyes, proteins, and imaging techniques to study mitochondrial dynamics in mammalian cells. Biophys Rep. 2017;3(4):64-72.

28.   Chaudhry A. Mitochondria Analyzer 2019 [Available from: https://github.com/AhsenChaudhry/Mitochondria-Analyzer]

29.   Hartig SM. Basic image analysis and manipulation in ImageJ. Curr Protoc Mol Biol. 2013;Chapter 14:Unit14 5.

30. Tseng Q. AdaptiveThreshold - ImageJ Plugin. [Available from: https://sites.google.com/site/qingzongtseng/adaptivethreshold#use]

701   31.   Landini   G,   ImageJ.   Auto   Local   Threshold.   [Available   from:
702   https://imagej.net/Auto_Local_Threshold]

703   32.   Anchang B, Hart TD, Bendall SC, Qiu P, Bjornson Z, Linderman M, et al. Visualization
704   and cellular hierarchy inference of single-cell data using SPADE. Nat Protoc. 2016;11(7):1264-
705   79.

706   33.   Qiu P, Simonds EF, Bendall SC, Gibbs KD, Jr., Bruggner RV, Linderman MD, et al.
707   Extracting a cellular hierarchy from high-dimensional cytometry data with SPADE. Nature
708   biotechnology. 2011;29(10):886-91.

709   34.   Berman SB, Chen YB, Qi B, McCaffery JM, Rucker EB, 3rd, Goebbels S, et al. Bcl-x L
710   increases mitochondrial fission, fusion, and biomass in neurons. J Cell Biol. 2009;184(5):707-19.

711   35.   Fouquet C, Gilles JF, Heck N, Dos Santos M, Schwartzmann R, Cannaya V, et al.
712   Improving axial resolution in confocal microscopy with new high refractive index mounting
713   media. PLoS One. 2015;10(3):e0121096.

714   36.   Cole RW, Jinadasa T, Brown CM. Measuring and interpreting point spread functions to
715   determine   confocal   microscope   resolution   and   ensure   quality   control.   Nat   Protoc.
716   2011;6(12):1929-41.

717   37.   Pawley J. Points, Pixels, and Gray Levels: Digitizing Imaging Data.   Handbook of
718   Biological Confocal Microscopy2006. p. 59-80.

719   38.   Imaging SV. Microscopy Nyquist rate and PSF calculator. [Available   from:
720   https://svi.nl/NyquistCalculator]

721   39.   Sage D, Donati L, Soulez F, Fortun D, Schmit G, Seitz A, et al. DeconvolutionLab2: An
722   open-source software for deconvolution microscopy. Methods. 2017;115:28-41.

723   40.   Wikstrom JD, Katzman SM, Mohamed H, Twig G, Graf SA, Heart E, et al. beta-Cell
724   mitochondria exhibit membrane potential heterogeneity that can be altered by stimulatory or toxic
725   fuel levels. Diabetes. 2007;56(10):2569-78.

726   41.   Sun MG, Williams J, Munoz-Pinedo C, Perkins GA, Brown JM, Ellisman MH, et al.
727   Correlated   three-dimensional   light   and   electron   microscopy   reveals   transformation   of
728   mitochondria during apoptosis. Nat Cell Biol. 2007;9(9):1057-65.

729   42.   Jakobs S. High resolution imaging of live mitochondria. Biochim Biophys Acta.
730   2006;1763(5-6):561-75.

731   43.   Zahedi A, On V, Phandthong R, Chaili A, Remark G, Bhanu B, et al. Deep Analysis of
732   Mitochondria and Cell Health Using Machine Learning. Sci Rep. 2018;8(1):16354.

733   44.   Leonard AP, Cameron RB, Speiser JL, Wolf BJ, Peterson YK, Schnellmann RG, et al.
734   Quantitative analysis of mitochondrial morphology and membrane potential in living cells using

735   high-content imaging, machine learning, and morphological binning. Biochim Biophys Acta.
736   2015;1853(2):348-60.

737   45.   Thivolet C, Vial G, Cassel R, Rieusset J, Madec AM. Reduction of endoplasmic reticulum-
738   mitochondria interactions in beta cells from patients with type 2 diabetes. PLoS One.
739   2017;12(7):e0182027.

740   46.   Valm AM, Cohen S, Legant WR, Melunis J, Hershberg U, Wait E, et al. Applying systems-
741   level spectral imaging and analysis to reveal the organelle interactome. Nature.
742   2017;546(7656):162-7.

743   47.   Han Y, Li M, Qiu F, Zhang M, Zhang YH. Cell-permeable organic fluorescent probes for
744   live-cell long-term super-resolution imaging reveal lysosome-mitochondrion interactions. Nature
745   communications. 2017;8(1):1307.

746   48.   Sandebring A, Thomas KJ, Beilina A, van der Brug M, Cleland MM, Ahmad R, et al.
747   Mitochondrial alterations in PINK1 deficient cells are influenced by calcineurin-dependent
748   dephosphorylation of dynamin-related protein 1. PLoS One. 2009;4(5):e5701.

749   49.   Aharoni-Simon M, Shumiatcher R, Yeung A, Shih AZ, Dolinsky VW, Doucette CA, et al.
750   Bcl-2 Regulates Reactive Oxygen Species Signaling and a Redox-Sensitive Mitochondrial Proton
751   Leak in Mouse Pancreatic beta-Cells. Endocrinology. 2016;157(6):2270-81.

752   50.   Luciani DS, Ao P, Hu X, Warnock GL, Johnson JD. Voltage-gated Ca(2+) influx and
753   insulin secretion in human and mouse beta-cells are impaired by the mitochondrial Na(+)/Ca(2+)
754   exchange inhibitor CGP-37157. Eur J Pharmacol. 2007;576(1-3):18-25.

755   51.   Kirshner H, Aguet F, Sage D, Unser M. 3-D PSF fitting for fluorescence microscopy:
756   implementation and localization application. J Microsc. 2013;249(1):13-25.

757   52.   Dey N, Blanc-Feraud L, Zimmer C, Roux P, Kam Z, Olivo-Marin JC, et al. Richardson-
758   Lucy algorithm with total variation regularization for 3D confocal microscope deconvolution.
759   Microscopy research and technique. 2006;69(4):260-6.

760   53.   Ollion J, Cochennec J, Loll F, Escude C, Boudier T. TANGO: a generic tool for high-
761   throughput 3D image analysis for studying nuclear organization. Bioinformatics.
762   2013;29(14):1840-1.

763   54.   Legland D, Arganda-Carreras I, Andrey P. MorphoLibJ: integrated library and plugins for
764   mathematical morphology with ImageJ. Bioinformatics. 2016;32(22):3532-4.
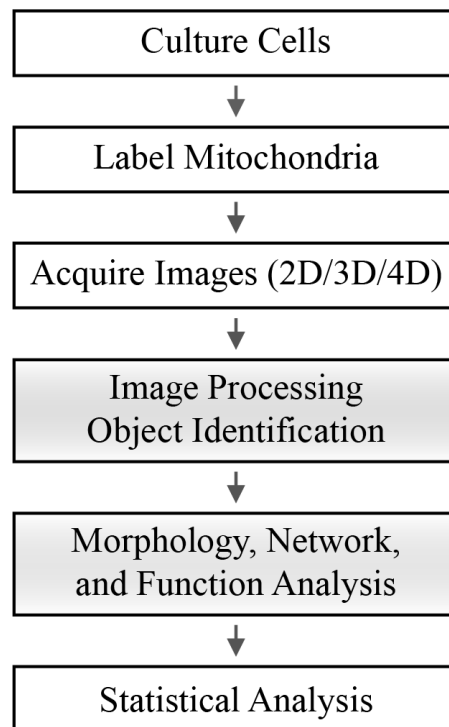
Chaudhry et al. – Figure 1

```
┌─────────────────────────────┐
│        Culture Cells        │
└─────────────────────────────┘
               ↓
┌─────────────────────────────┐
│      Label Mitochondria     │
└─────────────────────────────┘
               ↓
┌─────────────────────────────┐
│   Acquire Images (2D/3D/4D) │
└─────────────────────────────┘
               ↓
┌─────────────────────────────┐
│       Image Processing      │
│     Object Identification   │
└─────────────────────────────┘
               ↓
┌─────────────────────────────┐
│      Morphology, Network,   │
│     and Function Analysis   │
└─────────────────────────────┘
               ↓
┌─────────────────────────────┐
│     Statistical Analysis    │
└─────────────────────────────┘
```

Figure 1: **Schematic of the general workflow required for mitochondrial analysis by confocal microscopy**. The shaded boxes represent the steps that are addressed and detailed in this paper.

26

Chaudhry et al. – Figure 2
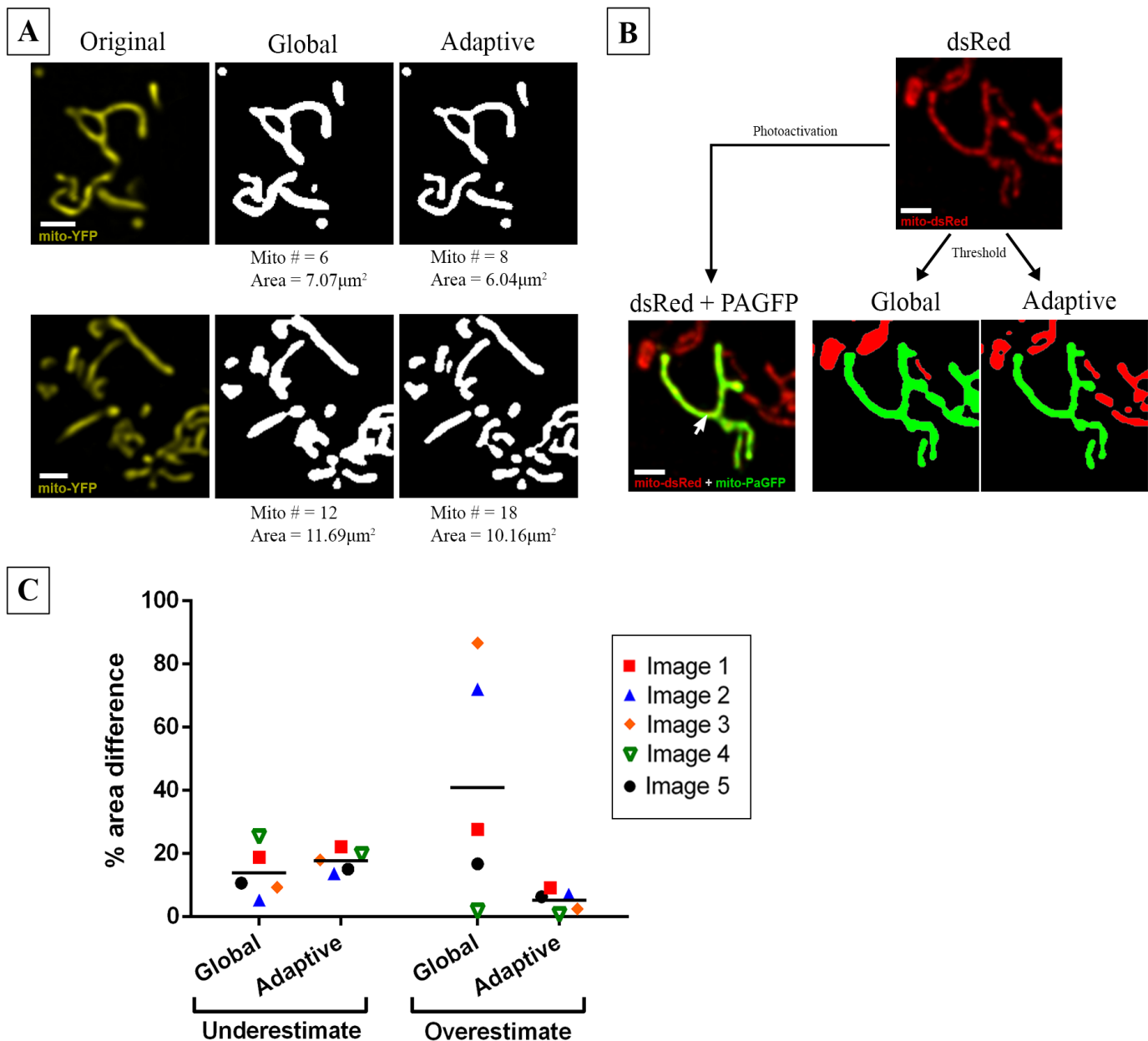
Figure 2: Comparison of mitochondrial identification using Global vs Adaptive thresholding methods. (**A**) Two representative examples of object identification using Global thresholding ('Default' method) vs Adaptive thresholding (radius = 1.25 μm, C = 11) on images of MIN6-cell mitochondria labelled with Mito-YFP. The number of identified objects (mitochondria) and their total area are indicated below the images. Scale bar = 1 μm. (**B**) Part of the mitochondrial network in a MIN6 cell co-transfected with mito-dsRed and mito-PAGFP. *Top* - All mitochondria imaged in the mito-dsRed channel. *Bottom left* - A single mitochondrion (green) was labeled by laser-based mito-PAGFP activation at the point indicated by the arrow. *Bottom right* - Object identification using Global vs Adaptive threshold algorithms applied to the dsRed channel; in each image, the object that is identified as contiguous with the PAGFP-labelled mitochondrion is shown in green. Comparison with the original image shows that the Adaptive method more accurately distinguished the photo-labeled mitochondrion, whereas Global thresholding artificially merged it with adjacent mitochondria. Scale bar = 1 μm. (**C**) Quantitative comparison of the degree to which Global and Adaptive thresholding under- or over-estimated the PAGFP-labeled mitochondrion in 5 test images. The corresponding images and details of the estimation algorithm are shown in Figure S3.

27

Chaudhry et al. – Figure 3

A

Morphology			
2D		**3D**	
Area	*Number of pixels.*	Volume	*Number of voxels.*
Perimeter	*Boundary pixel count*	Surface Area	*Estimate of area on surface.*
Form Factor	$\dfrac{P^2}{4\pi A}$ *1 (round),* *↑ with elongation.*	Sphericity	$36\pi\dfrac{V^2}{S^3}$ *0 (non-spherical)* *to 1 (spherical).*
Aspect Ratio	$AR = \dfrac{d_{max}}{d_{min}}$ *0 (round) to 1 (elongated).*		

B

Network / Connectivity
Branch Number
Branch Junctions
Branch Length
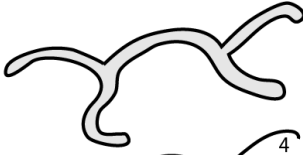
1 Branch	1 Branch	5 Branches
0 Branch Junctions	0 Branch Junctions	2 Branch Junctions
↓ Mean Branch Length	↑↑ Mean Branch Length	↑ Mean Branch Length
↓ Total Branch Length	↑ Total Branch Length	↑↑ Total Branch Length

Figure 3: Summary of morphological and network descriptors used in 2D/3D analysis of mitochondria. (A) Summary and definitions of the mathematical descriptors used to quantify mitochondrial morphology in two and three dimensions. **(B)** Summary of parameters used to describe mitochondrial network connectivity and illustration of skeletonization analysis on: a punctate object with no branch junctions and minimal branch length (*Left*); a long single tubular object with no branch junctions but higher branch length (*Middle*); and a complex object with multiple branches and junctions (gray dots), and the highest total branch length (*Right*). Note that the mean branch length, derived by dividing the total branch length by number of branches, is greater in the object in the middle than the more complex object on the right.
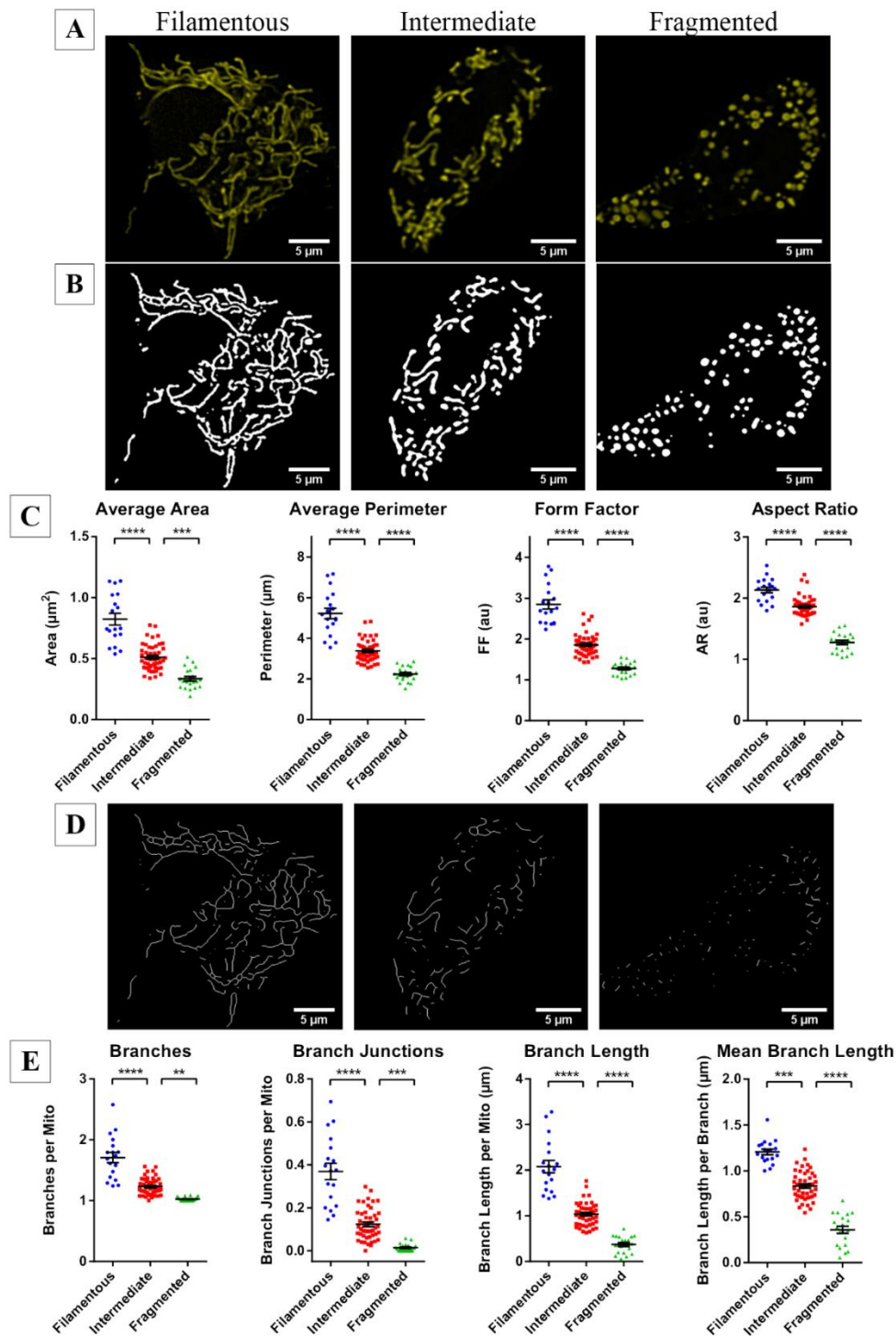
Chaudhry et al. – Figure 4

Figure 4: Quantitative comparison of mitochondrial morphology and network connectivity in 2D. Based on visual inspection of their mitochondria, 84 images of Mito-YFP-expressing MIN6 cells were categorized into three morphological groups: fragmented (20 cells), intermediate (46 cells), or filamentous (18 cells). **(A)** Examples of the YFP-labeled mitochondria in representative cells from each group, and **(B)** the objects identified by application of adaptive thresholding to the images. **(C)** The 2D morphological analysis of all cells in each of the categories. **(D)** Skeletonization of the mitochondrial objects identified in panel B. **(E)** Quantitative analysis and comparison of mitochondrial network connectivity performed on all cells in each morphological category. Data are represented by mean ± SEM. One-way ANOVA with Sidak post-hoc test was used to compare the groups; ***p<0.001, ****p<0.0001.

29

Chaudhry et al. – Figure 5
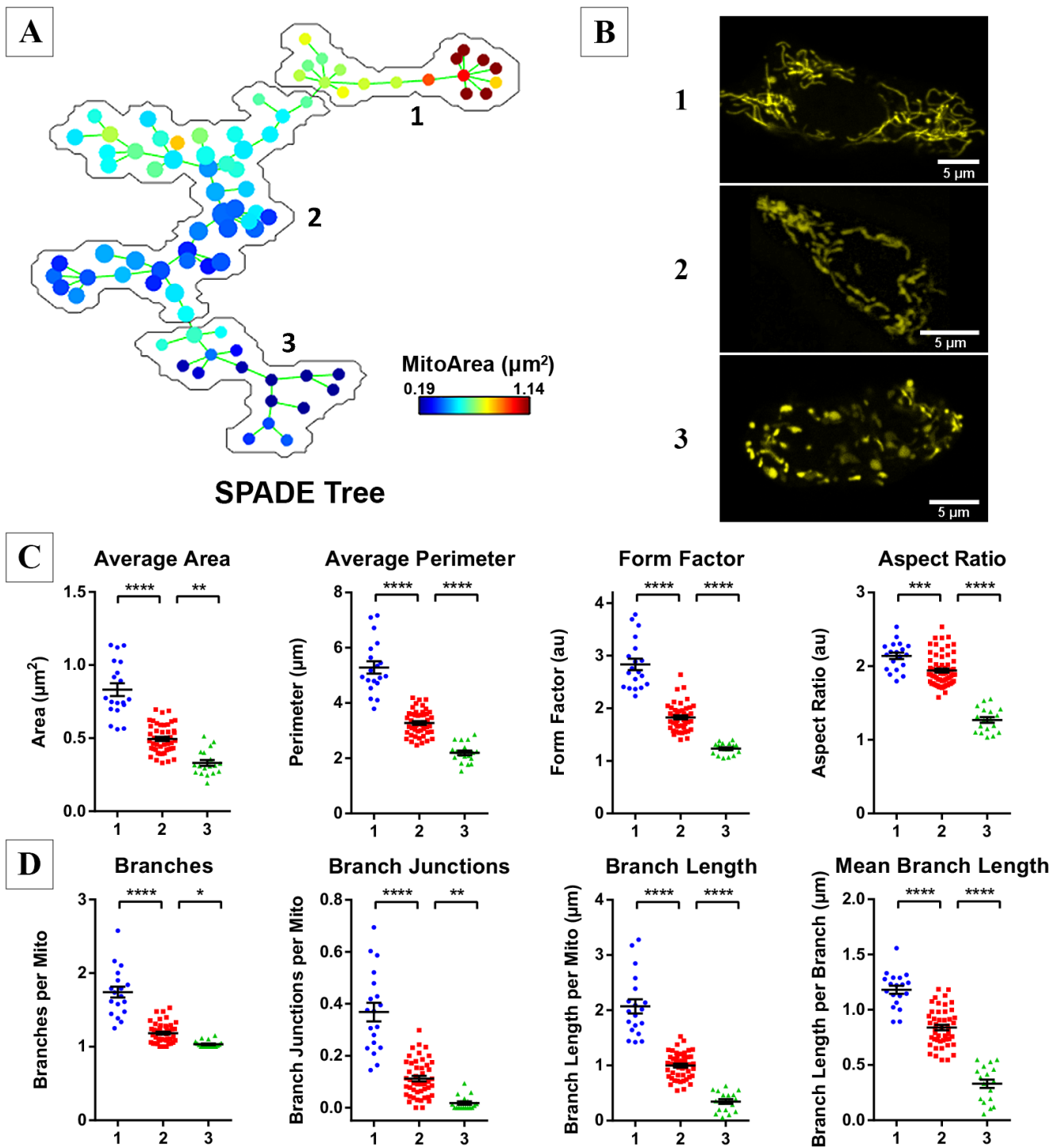
Figure 5: Unsupervised categorization of mitochondrial features using Spanning-tree Progression Analysis of Density-normalized Events (SPADE). (A) A SPADE tree was generated based on the same set of 84 images used in Figure 4, and then automatically subdivided into 3 groups; Group 1 contains 19 nodes/cells, Group 2 contains 47 nodes/cells, and Group 3 contains 18 nodes/cells. **(B)** Representative images extracted from each of the three SPADE-generated groups. **(C, D)** Comparison of the mitochondrial morphology and network parameters between the 3 SPADE-identified cell groups. All data are represented by mean ± SEM. *p<0.05, **p<0.01, ***p<0.001, ****p<0.0001 as determined by one-way ANOVA with Sidak post-hoc test; n=84 images.

30

Chaudhry et al. – Figure 6
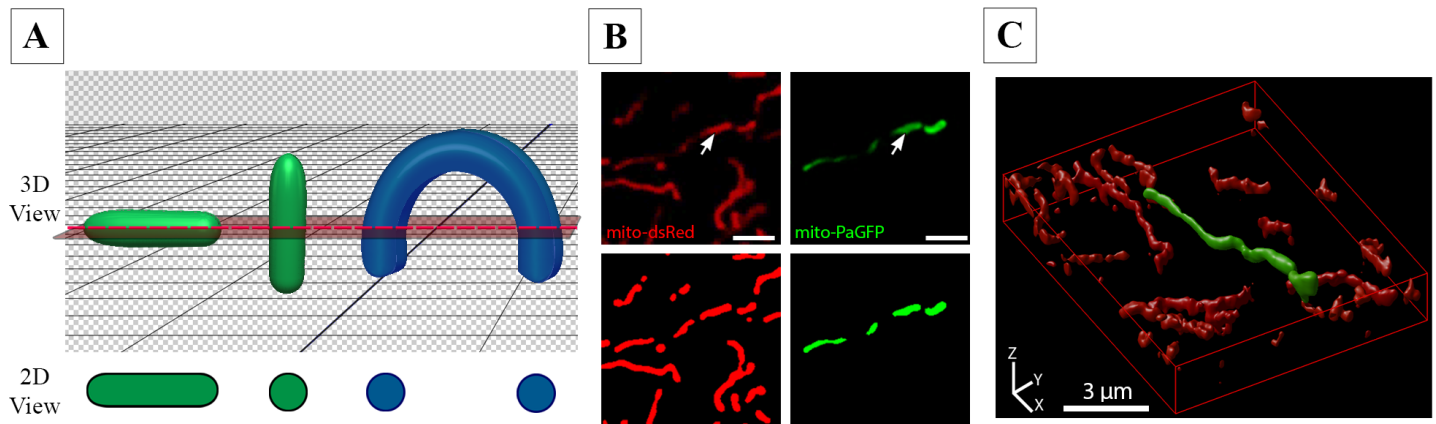
Figure 6: Limitations of 2D morphometric analysis. (A) Schematic illustrating the effect of object orientation in 3D space on the image capture in a horizontal 2D slice. The apparent 2D morphology of the same tubular object (shown in green) will depend on its orientation relative to the confocal plane. If a curved object (shown in blue) intersects the confocal plane at several locations, it will erroneously be identified as separate objects. **(B)** MIN6 cells were co-transfected with Mito-dsRed and Mito-PAGFP and photoactivation induced at the point indicated by an arrowhead. Scale bars = 3 µm. *Top row* – 2D image of Mito-dsRed and mito-PAGFP channels after photoactivation. *Bottom row* – objects identified after pre-processing and thresholding of the 2D cross-section. **(C)** Full 3D imaging and reconstruction (rendered using Huygens Professional software) of the same mitochondrial population shown in panel B. Note that the photo-labelled mitochondrion in 2D appears as a series of separate mitochondria, whereas 3D visualization correctly identifies it as one contiguous organelle.
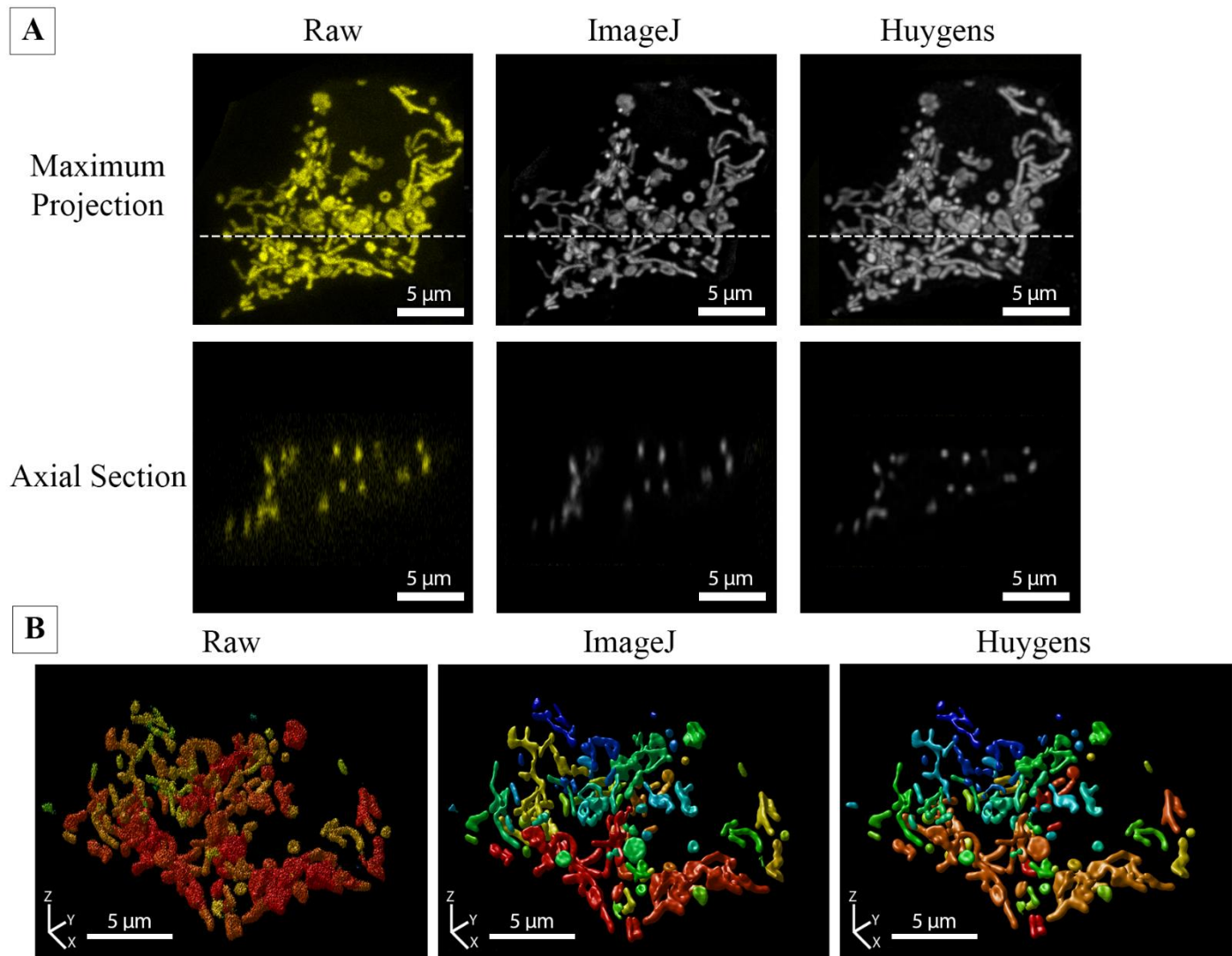
Chaudhry et al. – Figure 7

Figure 7: Deconvolution improves the quality and accuracy of 3D mitochondrial analysis. (A) A full z-stack was acquired from a Mito-YFP-expressing MIN6 cell that was 11 μm in height. *Top Panel* – Maximum projection views of the z-stack before and after deconvolution. The confocal image stack was deconvolved using either ImageJ DeconvolutionLab (Richardson-Lucy algorithm) or Huygens Professional (Classical Maximum Likelihood Estimation) software for 40 iterations. The dotted line indicates the position of the axial section shown below. *Bottom Panel* – Axial sections (*xz*-plane) of the raw and deconvolved image stacks. The reduction in axial stretching of objects can be seen in the deconvolved stacks, with the best improvement achieved using the Huygens algorithm (see additional details in Figure S5 and Supplemental Table S1). **(B)** 3D renderings of the z-stack before and after deconvolution with ImageJ or Huygens Professional. All 3D visualizations were generated using the Huygens 3D object renderer, with a unique colour assigned to separate objects.
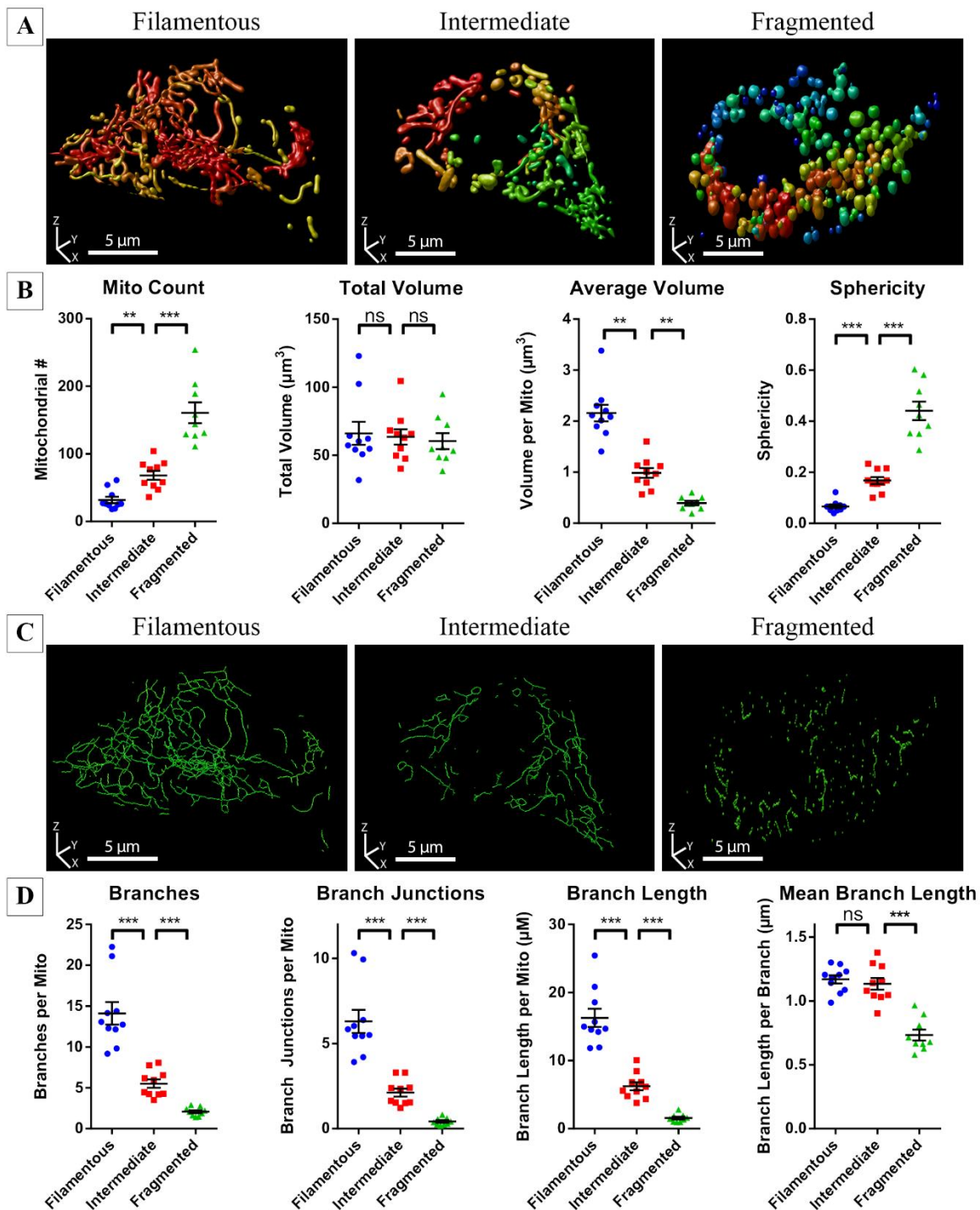
Chaudhry et al. – Figure 8

Figure 8: Quantitative comparison of mitochondrial morphology and network connectivity in 3D. Image stacks of Mito-YFP-expressing MIN6 cells were visualized in 3D and their mitochondria manually categorized as fragmented, intermediate or filamentous. **(A)** 3D renderings (produced using Huygens Professional) of representative Mito-YFP-expressing MIN6 cells from each of the morphological categories. **(B)** Quantitative 3D analysis and comparison of mitochondrial morphology between cells in each category. **(C)** 3D renderings of the skeletonized mitochondrial network of the cells depicted in panel A. **(D)** Quantitative 3D analysis and comparison of mitochondrial network connectivity between cells in each category. All data are represented by mean ± SEM. *p<0.05, **p<0.01, ***p<0.001, as determined by one-way ANOVA with Sidak post-hoc test. N=10 cells in each category.
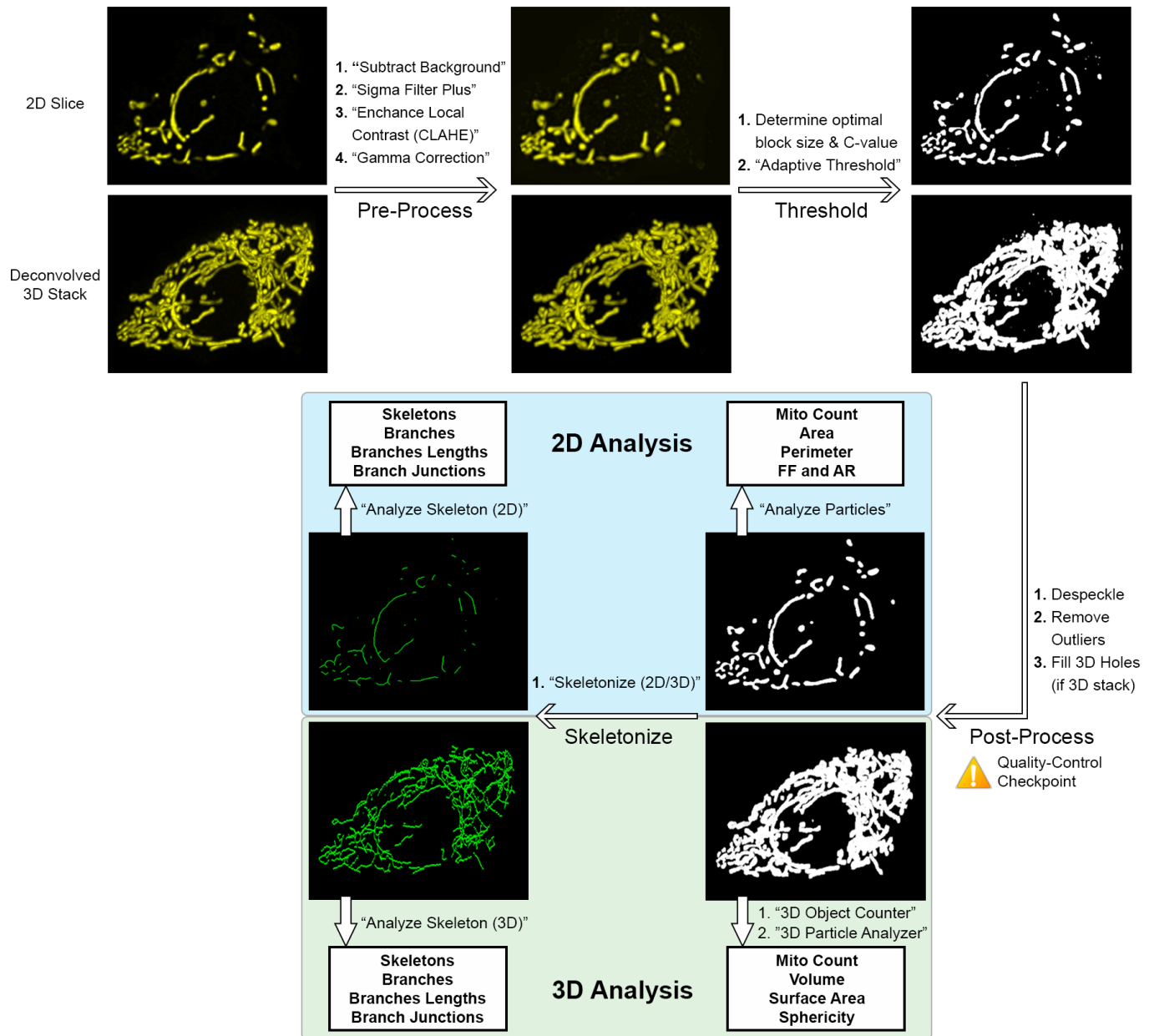
33

Chaudhry et al. – Figure 9

Figure 9: Summary of pipeline for 2D and 3D mitochondrial analysis in ImageJ/Fiji. For illustration, an image stack was acquired from a MIN6 cell expressing Mito-YFP; a representative slice is shown as the 2D input, and the entire stack (after deconvolution) as the 3D input. 3D Stacks are represented as maximum projections here. Scale bars = 5 μm. See main text and Materials & Methods for additional details and parameter values.

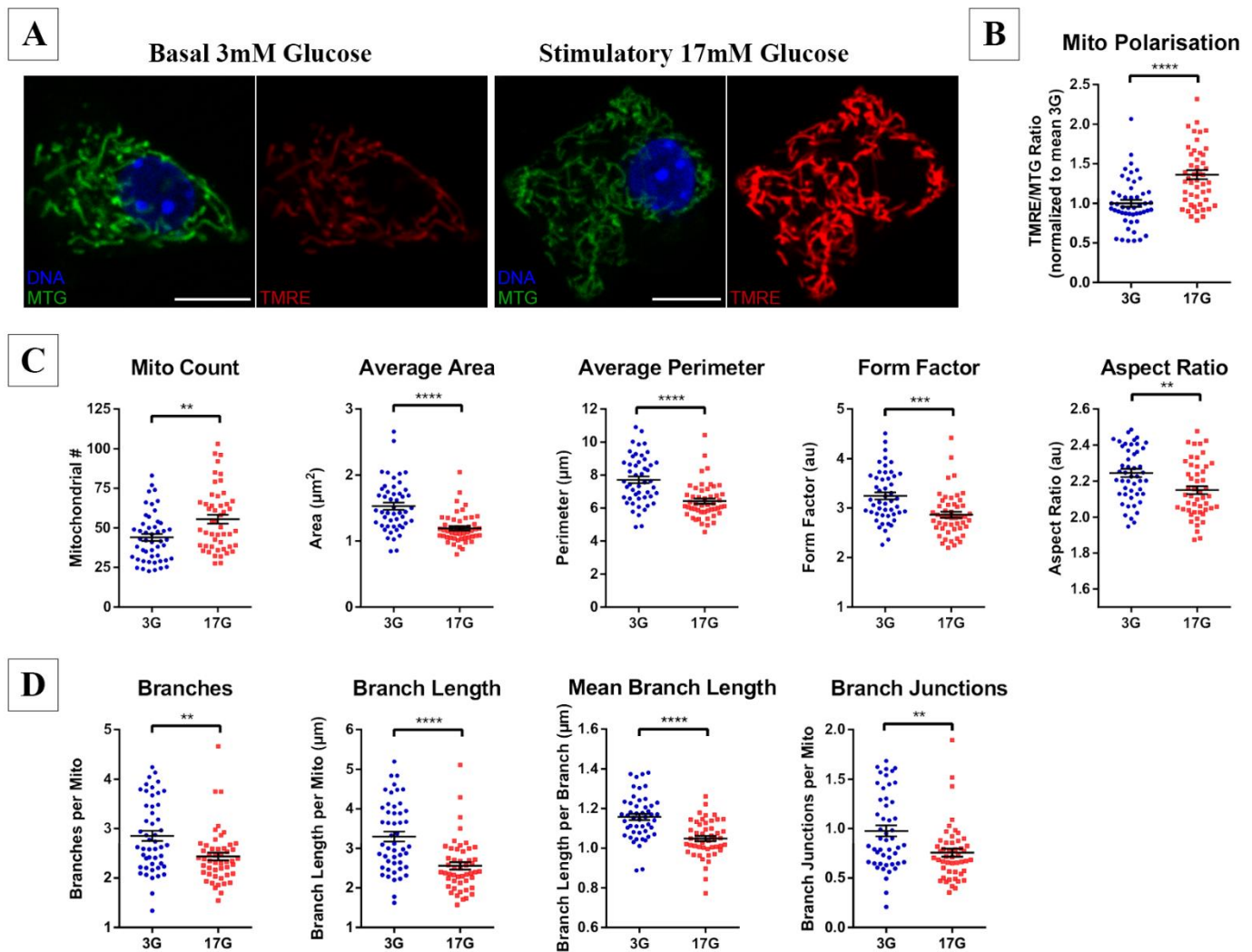## Chaudhry et al. – Figure 10

Figure 10: Two-dimensional analysis shows that glucose stimulation is associated with mitochondrial fission in pancreatic islet cells. Dispersed mouse islet cells were treated in either 3mM glucose (3G) or 17mM glucose (17G) for 60 minutes and then labeled with Hoescht 33342, MitoTracker Green FM (MTG), and TMRE before 2D imaging. **(A)** Representative images of a MTG and TMRE stained islet cell in 3G and 17G. **(B)** TMRE/MTG ratio (normalized to average 3G), indicating the degree of mitochondrial hyperpolarisation. Mitochondrial morphology and polarization were quantified using our 2D analysis pipeline in Fiji/ImageJ (see Materials and Methods). Comparison of mitochondrial morphometry **(C)**, and mitochondrial network connectivity **(D)** demonstrates significant differences between cells acutely treated with low and stimulatory glucose. All data are represented by mean ± SEM. **p<0.01, ***p<0.001, ****p<0.0001 as determined by Student's t-test; n=49 cells in each glucose treatment from 4 mice.
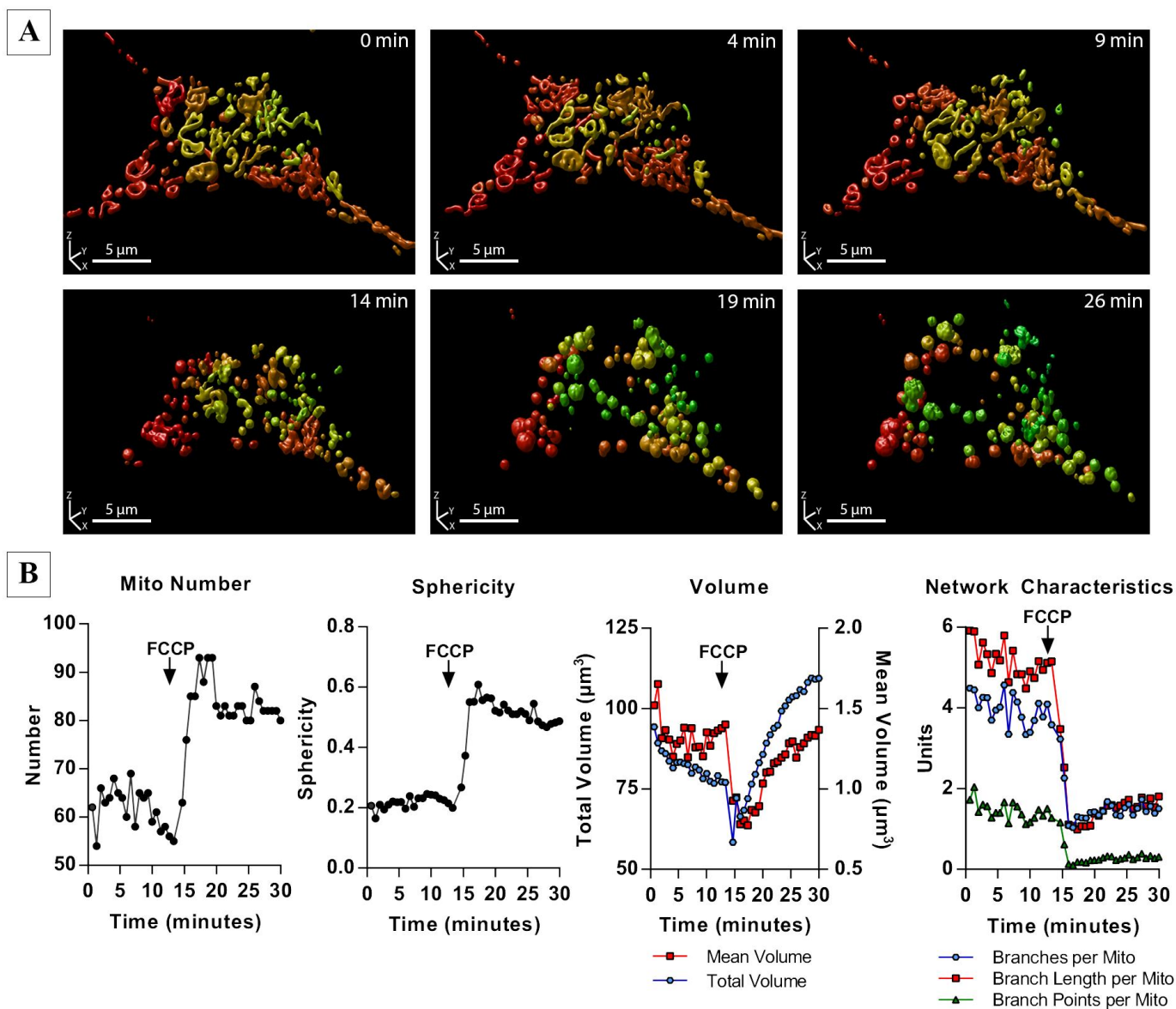
Chaudhry et al. – Figure 11

Figure 11: Time-lapse 3D imaging (*xyzt*) and analysis of mitochondrial dynamics. Mito-YFP-expressing MIN6 cells were imaged in a stage-top incubator with one full image stack acquired every minute. **(A)** 3D renderings (produced in Huygens Professional) of the mitochondrial network in a single cell at different time-points. A high concentration FCCP (25 µM) was added to the incubation media around the 13-minute mark. **(B)** Quantitative analysis of the time-dependent effects of FCCP on mitochondrial number, sphericity, total and mean volume, and network characteristics in the cell.